Nanoscale insights on phase transition dynamics of doped VO₂ for memristor devices 🅕 ✅

Lin Wang (王林) ⓘ ; Li Chen (陈立); Xionghu Xu (许雄虎); Zhangchen Hou (侯张晨) ⓘ ; Yafang Li (李亚芳); Liyan Shang (商丽燕) ⓘ ; Jinzhong Zhang (张金中) ⓘ ; Liangqing Zhu (朱亮清) ⓘ ; Yawei Li (李亚巍) ⓘ ; Fei Cao (曹菲); Genshui Wang (王根水) ⓘ ; Junhao Chu (褚君浩); Zhigao Hu (胡志高) ✉ ⓘ

Check for updates

View Online   Export Citation

Articles You May Be Interested In

Light-controlled stateful reconfigurable logic in a carbon dot-based optoelectronic memristor

Appl. Phys. Lett. (February 2024)

Improvement of forming-free threshold switching reliability of CeO₂-based selector device by controlling volatile filament formation behaviors

APL Mater. (May 2022)

Dual-layer volatile memristor with ultralow voltage slope

Appl. Phys. Lett. (March 2024)

Nanoscale insights on phase transition dynamics of doped VO₂ for memristor devices ⓕ

Lin Wang (王林),[1] ⓘ Li Chen (陈立),[1] Xionghu Xu (许雄虎),[1] Zhangchen Hou (侯张晨),[1] ⓘ Yafang Li (李亚芳),[1]
Liyan Shang (商丽燕),[1] ⓘ Jinzhong Zhang (张金中),[1] ⓘ Liangqing Zhu (朱亮清),[1] ⓘ Yawei Li (李亚巍),[1] ⓘ Fei Cao (曹菲),[2]
Genshui Wang (王根水),[2] ⓘ Junhao Chu (褚君浩),[1,3] and Zhigao Hu (胡志高)[1,3,a] ⓘ

AFFILIATIONS

[1]Technical Center for Multifunctional Magneto-Optical Spectroscopy (Shanghai), Engineering Research Center of Nanophotonics &
  Advanced Instrument (Ministry of Education), Department of Physics, School of Physics and Electronic Science, East China Normal
  University, Shanghai 200241, China
[2]The State Key Lab of High Performance Ceramics and Superfine Microstructure & The Key Lab of Inorganic Functional Materials
  and Devices, Shanghai Institute of Ceramics, Chinese Academy of Sciences, 200050 Shanghai, China
[3]Collaborative Innovation Center of Extreme Optics, Shanxi University, Taiyuan, Shanxi 030006, China

[a]Author to whom correspondence should be addressed: zghu@ee.ecnu.edu.cn

ABSTRACT

This study utilized co-sputtering to fabricate Mo-doped VO₂ films and identified an optimal concentration exhibiting a lower phase transition temperature ($T_h = 55.8\,°C$) and a broader hysteresis window ($\Delta T = 13.6\,°C$). At the atomistic scale, it is demonstrated that Mo dopant-induced localized strain accelerates the phase transition, which leads to the relaxation of the tetragonal structure. Furthermore, the effects of Mo doping on the phase transition process and electrical properties are characterized at the nanoscale using conductive atomic force microscopy and Kelvin probe force microscopy, and the potential application in selectors can be evaluated. The results indicated that Mo doping destabilizes the M1 phase by introducing a high density of electrons, thereby significantly reducing the electron–electron interactions as per the Mott model. Moreover, the device exhibited stable threshold and memristive properties at room temperature, quickly switching from high to low-resistance states at a threshold voltage of 2.37 V and maintaining stability over more than 1000 cycles with a selectivity $>10^2$. The present work not only highlights the role of Mo doping in enhancing the functional properties of VO₂ but also demonstrates its feasibility in high-performance selectors devices.

I. INTRODUCTION

Vanadium dioxide (VO₂) has become a focal point for the study of the metal-to-insulator transition (MIT) near room temperature,[1–3] captivating the interest of researchers for its potential applications in smart electronics.[4,5] Characterized by a reversible phase transition from an insulating monoclinic phase to a conductive tetragonal rutile phase, VO₂ exhibits a remarkable sensitivity to external stimuli, including temperature, electric fields, and mechanical stress.[6,7] It also has the ability to dynamic switching between high-resistance (HRS) and low-resistance states (LRS).[2,8–11] This unique behavior underpins its promise for innovative applications in optoelectronic switches,[12,13] memory devices,[14] and sensors.[15,16] As a specialized type of memristor device, selectors leverage threshold switching behavior to emulate neural pulse responses and probabilistic behavior, making them critical for neuron circuits and synaptic simulations in neuromorphic systems.[17,18]

Traditional VO₂-based devices struggle with low-power electronics demands due to the necessary high phase transition temperature for an effective MIT. Furthermore, high operating voltages and concerns over stability and reliability further limit their application, particularly in energy-efficient settings.[19,20] Therefore, enhancing the energy efficiency of VO₂ switch devices, particularly in memory and switching technologies, is crucial to overcome these limitations and expanding their practical applications.

Current research efforts focus on enhancing VO₂-based devices by manipulating the oxygen partial pressure and device architecture.[20,21] Adjusting oxygen vacancies has been showed to facilitate the MIT of VO₂ at lower voltages, preserving this capability across nano to micrometer scales.[6] Localized heating through nanoscale heaters has induced the MIT at 24 V while maintaining a low switching power of approximately 85 μW.[22] Despite these advancements in addressing

high power consumption, the persistent challenge of high phase transition temperatures (T_{MIT}) remains unresolved. Doping has been established as an effective strategy for modifying the T_{MIT} and enhancing the physical properties of VO_2.[20,23] Milinda Pattanayak et al.[24] designed a W-doped VO_2-based spontaneous electric oscillator, achieving threshold switching at 35 V. Similarly, Ling Chen et al.[25] employed thermally driven voltage biases, enabling W-doped VO_2 films to exhibit threshold switching characteristics at 5 °C and 4 V. Rupp et al.[26] developed threshold switching behavior in VO_2 crossbar selectors based on Cr doping. Although W and Cr doping adeptly modifies the T_{MIT}, it inadvertently compromises the electrical switching efficiency and leads to poor reproducibility of VO_2. Although W doping adeptly modifies the T_{MIT}, it inadvertently compromises the electrical switching efficiency of VO_2.[15,27] In contrast, Mo doping emerges as a superior alternative, simultaneously enhancing the electrical transport characteristics and reducing the T_{MIT} from 68 °C to 43.18 °C.[8,28,29] This approach not only enhances the electronic structure and micro-morphology[30] but also advances the discourse on the electronic behaviors and phase transition mechanisms within Mo-doped VO_2 films.

In this work, we fabricated VO_2 films with Mo dopant to achieve a lower phase transition temperature ($T_h = 55.8$ °C) and an expanded hysteresis window ($\Delta T = 13.6$ °C), aiming to explore their potential applications in selectors. Using aberration-corrected scanning transmission electron microscopy (STEM), we revealed the atomic scale mechanisms of the phase transition by Mo doping in VO_2 films. Atomic-resolution strain maps allowed us to analyze how local strain induced by doping accelerates the phase transition. Utilizing conductive atomic force microscopy (C-AFM), we characterized the electrical properties and phase transition behaviors of Mo-doped VO_2 films at the nanoscale. It demonstrated that Mo doping disrupted the stability of the M1 phase of VO_2 by increasing the electron density. Additionally, the films were able to swiftly switch from a HRS to a LRS at a threshold voltage (V_{th}) of 2.37 V and reliably returned to the HRS at a holding voltage (V_{hold}) of 1.25 V during the reverse scan. After more than 1000 cycles, the selectors showed a selectivity greater than 10^2 and maintained a stable resistance state. These results provide significant theoretical and experimental supports for the development of high-performance selectors at room temperature.

II. MATERIALS AND METHODS

A. Material fabrications

Mo-doped VO_2 thin films were prepared by magnetron sputtering deposition using a co-sputtering technique. V target (99.99%) and Mo target (99.99%) materials were deposited onto Si/SiO_2 substrates.[40] Prior to deposition, the substrates were cleaned with acetone and ethanol, rinsed with deionized water, and dried. The deposition was carried out in a chamber at a pressure of 0.6 Pa, with a mixture of Ar and O_2 gases injected into the chamber. The sputtering power for the V target was set to 60 W, and the doping concentration was controlled by adjusting the sputtering power for the Mo target. The as-deposited amorphous films were annealed at 450 °C in argon gas for 1 h to obtain crystalline $Mo_xV_{1-x}O_2$ films.

B. Characterization of phase and microstructure

X-ray diffraction (XRD) was used to determine the crystal structure and phase purity of the films. Temperature-dependent Raman spectra were measured to probe the vibrational modes of the film on a micro-Raman spectrometer (Jobin-Yvon LabRAM HR 800 UV). In situ STEM images were obtained using an aberration-corrected transmission electron microscope (ACTEM) (JEM-ARM300F, acceleration voltage up to 300 kV). Atomic force microscopy (AFM) was used to examine the surface morphology of the films. Conductive atomic force microscopy (C-AFM) was used to measure and visualize the changes in surface current of films at different temperatures. Kelvin probe force microscopy (KPFM) was used to measure the work function differences and potential changes on the surface of devices. X-ray photoelectron spectroscopy (XPS) was used to analyze the chemical states and composition of the films.

C. Electrical measurements

Electrical measurements of the device were performed using a Keithley 4200-SCS semiconductor parameter analyzer.

D. First-principles calculations

All calculations were performed using the density functional theory (DFT), as implemented in the Vienna ab initio simulation package.[31,32] The projector augmented-wave (PAW) method and Perdew–Burke–Ernzerhof generalized gradient approximation (GGA-PBE) were used for the exchange correlation functionals.[33,34] As the d orbitals of Mo may have important correlation effects, we also validated our results using the GGA + U method. These include the Hubbard parameter U (which mirrors the strength of the on-site Coulomb interaction) and parameter J (which corrects the strength of the exchange interaction). In the somewhat simplified, yet rotationally invariant, method of Dudarev,[35] an effective interaction parameter $U_{eff} = U - J$, or simply U, can be introduced. Here, we used $U_{eff} = 3.4$ to derive the exact electronic structure of the ground state, a value that was determined to be a robust consideration.[36,37] Brillouin zone integration was performed using a $3 \times 3 \times 3$ Monkhorst–Pack k-point with a $2 \times 2 \times 2$ supercell.[38] Geometric optimization was performed using a conjugate gradient method until the energy converged at 1×10^{-5} eV and the convergence criterion of the largest force acting on the atoms was 0.03 eV/Å.

III. RESULTS AND DISCUSSION

To explore the impact of varying Mo doping concentrations on the structural properties of VO_2, Mo-doped VO_2 thin films (S0–S7) were prepared by co-sputtering, as detailed in Table I. Figure 1(a) shows the X-ray diffraction (XRD) spectra of the $Mo_xV_{1-x}O_2$ films at room temperature. The diffraction peak was observed at $2\theta = 27.8°$, matching the (011) plane of the monoclinic phase (M1) of VO_2 (JCPDS No.72-0514). Increasing Mo doping concentration led to a shift of the diffraction peak toward the tetragonal rutile (R) structure. Furthermore, variable temperature XRD spectra performed on S4 confirmed the temperature-dependent shift of the main peak, indicating the transition from the M1 to R phase (as shown in Fig. S1).

Figure 1(b) displays the Raman spectra of the films with typical Mo doping concentration at 25 °C. The A_g phonon modes are located at approximately 193, 223, 337, 387, 498, and 611 cm^{-1}, while the weaker peaks around 260, 303, and 442 cm^{-1} correspond to B_g phonon modes, respectively. The distinct peaks at 193, 223, and 611 cm^{-1} confirm the presence of a high-quality crystalline M1 phase, aligning with previous reports and underscoring the consistency of our

TABLE I. Different doping concentration and the T_{MIT} of $Mo_xV_{1-x}O_2$ films.

Sample	Formula	Power (W)	Mo (Atom%)	T_h (°C)	T_c (°C)	ΔT (°C)	T_{MIT} (°C)
S0	VO_2	0:60	0	73.8	65.5	8.3	69.7
S1	$Mo_{0.009}V_{0.991}O_2$	2:66	0.24	63.2	53.8	9.4	58.1
S2	$Mo_{0.014}V_{0.986}O_2$	1:60	0.36	60.5	49.5	11	55.0
S3	$Mo_{0.018}V_{0.982}O_2$	2:64	0.44	58.4	46.3	12.1	52.4
S4	$Mo_{0.021}V_{0.979}O_2$	2:62	0.54	55.8	42.2	13.6	49.0
S5	$Mo_{0.023}V_{0.978}O_2$	2:60	0.57	50.9	38.7	12.2	44.8
S6	$Mo_{0.026}V_{0.974}O_2$	3:60	0.68	42.6	32.1	10.5	37.4
S7	$Mo_{0.039}V_{0.961}O_2$	4:60	0.95	$\cdots$	$\cdots$	$\cdots$	$\cdots$
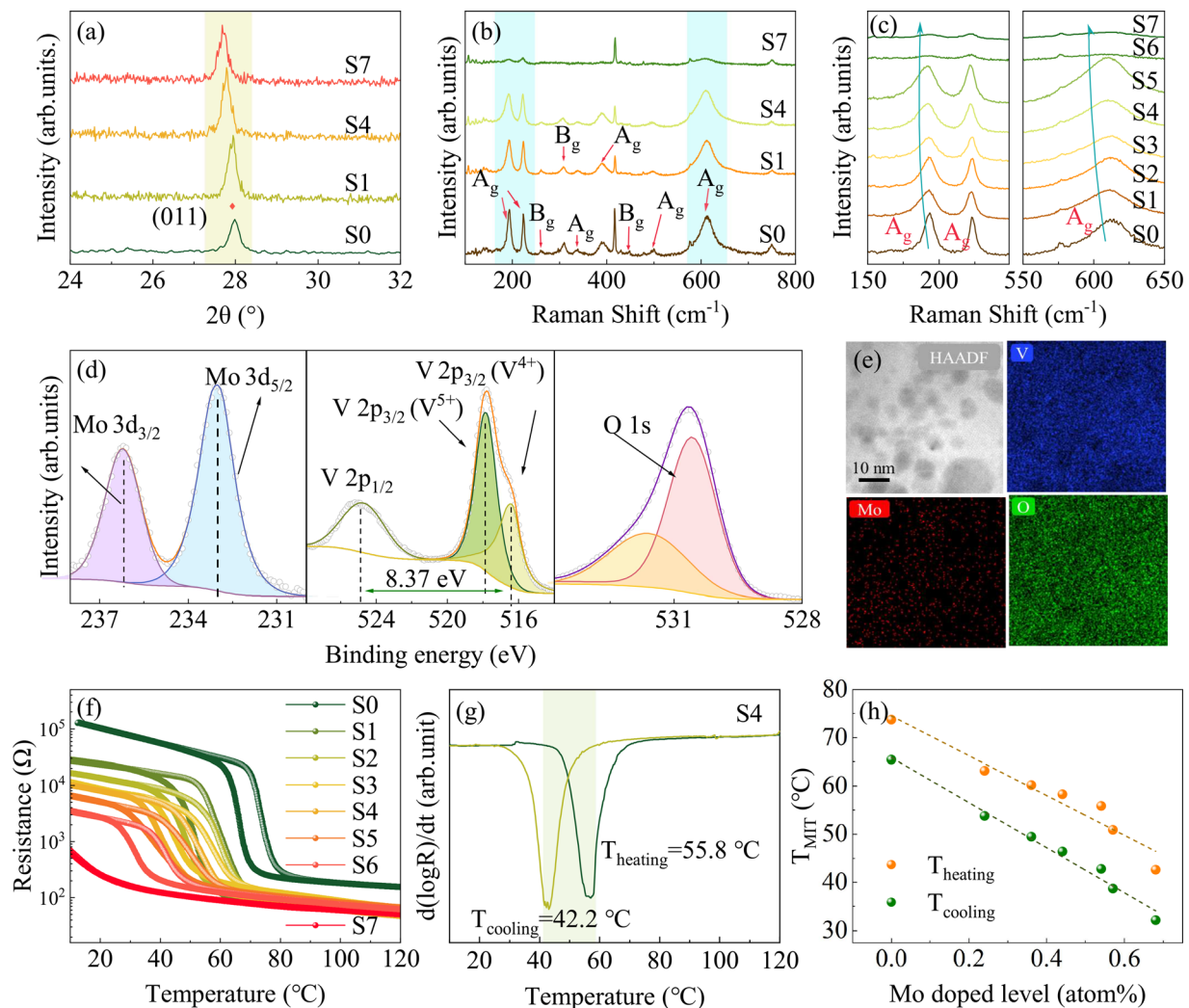
FIG. 1. Comprehensive characterization of $Mo_xV_{1-x}O_2$ films at room temperature. (a) XRD spectra of typical $Mo_xV_{1-x}O_2$ films (S0, S1, S4, and S7). (b) Raman spectra of typical $Mo_xV_{1-x}O_2$ film. (c) Magnified view of A_g phonon mode for all $Mo_xV_{1-x}O_2$ films. (d) XPS spectra of the sample S4, corresponding to V 2p, Mo 3d, and O 1s. (e) EDS map of a cross section of the sample S4 (in the focused ion beam-cut TEM lamella). (f) Temperature-dependent resistance (R–T) of all Mo-doped VO_2. Testing the heating and cooling process, respectively. (g) d(log(R))/dT curves of the sample S4. (h) T_{MIT} values for heating and cooling processes at different Mo doping levels.

findings.[39,40] We further investigated the changes in the Raman phonon peak of the films during the MIT process (as shown in Fig. S2). The characteristic phonon vibrations in the Raman spectra gradually weakened and eventually vanished as the temperature increased, indicating a transition from the M1 to R phase. Figure 1(c) shows the detailed variations in the principal phonon mode peaks of $Mo_xV_{1-x}O_2$ films as a function of Mo doping concentration. Notably, the two A_g phonon modes at 193 and 223 cm^{-1} are associated with the displacement of V ions along dimer chains, exhibiting a redshift and intensity weakening with increased doping levels. Moreover, the A_g phonon mode at 614 cm^{-1}, which reveals the characteristics of V–O vibrations, similarly displays a redshift. These spectral changes indicate that Mo doping results in an elongation of V–O bonds and a distortion of the VO_2 lattice, which can affect the dimeric interactions and V–O vibrations. Thus, it can lead to a decrease in phonon mode frequency and a shift to lower energies.

Figure 1(d) displays the V $2p_{3/2}$ spectral peaks predominantly showcased V^{4+} (515.9–516.4 eV) and V^{5+} (516.8–517.7 eV) peaks of sample S4. Compared with undoped VO_2 (as shown in Fig. S3), V^{3+} peaks were not observed in Mo-doped samples, signifying the substantial impact of Mo doping on the distribution of V valence states. This result is probably owing to the increase of oxygen vacancies by Mo doping. This increase in V^{4+} and V^{5+} states is attributed to the rise in oxygen vacancies induced by Mo doping. Specifically, the introduction of Mo^{6+} into the VO_2 lattice creates a local charge imbalance, leading the lattice to compensate by forming oxygen vacancies.[41] This vacancy formation not only stabilizes higher V oxidation states but also aligns with the observed shift in peak positions.

Besides, the emergence of V^{5+} peaks, associated with the surface oxygen composition, suggests that Mo doping could lead to an increase in oxygen vacancies and over-oxidation of V in VO_2. Combined with Fig. S4, it is observed that with an increase in Mo^{6+} doping, the central fitting peak of V $2p_{3/2}$ converged at 516.5 eV, while the V $2p_{1/2}$ peaks shifted toward higher binding energies. Moreover, the energy gap between $2p_{3/2}$ (V^{4+}) and V $2p_{1/2}$ widened from 7.76 to 9.25 eV, potentially reflecting alterations in the electronic structure and local chemical environment due to Mo doping. The Mo 3d spectral peaks across varying Mo doping concentrations were divided into Mo $3d_{3/2}$ and Mo $3d_{5/2}$, positioned at 232.7–233.0 and 235.9–236.1 eV, respectively, which are both attributed to the Mo^{6+} state. As Mo concentration increases, the intensity of Mo 3d peaks strengthens, indicating successful integration of Mo^{6+} and likely leading to lattice distortion and charge redistribution. As shown in Fig. S5, the peak at 530.1 eV primarily corresponds to lattice oxygen (O^{2-}), while the peak at 530.7 eV is related to oxygen vacancies or surface-adsorbed oxygen species (such as OH^- or H_2O). With increased Mo doping, the 530.1 eV peak weakens, and the 530.7 eV peak strengthens, indicating that Mo doping promotes oxygen vacancy formation and surface adsorption. The enhancement of the 530.7 eV peak provides direct evidence that Mo^{6+} induces oxygen vacancies through a charge compensation mechanism. These findings reveal the complex impact of Mo doping on the valence states and surface chemical states of VO_2, likely stemming from the electronic structure reorganization and lattice distortions induced by the incorporation of Mo^{6+}.[8,29]

As can be seen from the results of the energy dispersive X-ray spectra (EDS) in Fig. 1(e), the dispersion of Mo is relatively homogeneous in representative regions of the cross section. For exploring the

influence of Mo doping on the electrical characteristics of VO_2 films, the temperature-dependent resistance of typical samples is displayed in Fig. 1(f) (including heating and cooling processes). As Mo doping concentration is increased, the sharpness of resistance changes associated with the MIT and the M1 phase noticeably decreased. At sufficient doping levels, the MIT phenomenon completely vanishes, likely due to the significant alteration of the VO_2 lattice structure induced by the excess Mo^{6+}. The T_{MIT} (including the T_h and the T_c) were calculated by the formula Min $(d(logR)/d(T))$ and are displayed in Figs. 1(g) and S6. The T_h, T_c, and thermal hysteresis width (ΔT) data of all samples were extracted and displayed in Table I. Figure 1(h) displays the T_{MIT} of all samples. The T_{MIT} decreased with increasing dopant concentrations, indicating that doping enhances the conductivity. The observed effects could be due to lattice distortions induced by Mo^{6+}, which impact the electronic band structure and the distribution of electrons within the lattice. Additionally, the doping may introduce extra defects and impurity states into the lattice, which act as electron traps, further reducing electron mobility. The combined impact of these factors is sufficient to suppress or even eliminate the MIT, thereby altering the phase transition characteristics and resistive switching behavior of VO_2. However, the larger phase transition thermal hysteresis loops offer the possibility of achieving selectors of VO_2 devices near room temperature. Therefore, to further analyze the effect of Mo doping on VO_2, we selected sample S4 ($Mo_{0.021}V_{0.979}O_2$, $T_h = 55.8\,°C$, $\Delta T = 13.6\,°C$) for subsequent characterization and testing.

Figure 2(a) presents an atomic-resolution high-angle annular dark-field (HAADF) image, where the ordered arrangement of atoms is clearly visible. The uniform distribution of bright spots indicates that Mo dopant has not disrupted the overall crystal structure. The image marks different interplanar spacings, specifically $d = 3.333$, 2.49, and 2.552 Å, corresponding to the (-111), (-202), and (-102) planes, respectively. In Fig. 2(b), the fast Fourier transform (FFT) of the HAADF image confirms that the zone axis of the monoclinic $Mo_xV_{1-x}O_2$ structure is along $[-11-1]$. The clear spots in the FFT image indicate good crystal quality and periodic structure. Figure 2(c) shows a simulated diffraction pattern based on the $[-11-1]$ zone axis. Compared with the experimental FFT image, the spot positions and symmetry are largely consistent. Figures 2(d) and 2(e) display the intensity profiles for areas 1 and 2 in Fig. 2(a), respectively. The Mo atoms are larger than V atoms and cause lattice expansion upon substitution, thus altering the interatomic distances. Comparing two areas, the interatomic distance changes indicate non-uniform strain distribution due to Mo doping. This non-uniform strain may result from the random substitution of V atoms by Mo atoms, leading to localized stress concentration. Such stress concentration can induce local defects or distortions, consequently altering the phase transition characteristics and electrical properties of the film.

To reveal the impact of Mo doping on local strain and lattice distortion, we performed geometric phase analysis (GPA) on the atomic-resolution image in Fig. 2(a). GPA is a strain measurement method based on the Fourier transform. The distribution of strain and stress is quantified by extracting phase information from HRTEM images,[42] Figs. 2(f) and 2(g) show the in-plane strain (ε_{xx}) and out-of-plane strain (ε_{yy}) along the (-101) plane, respectively. The red regions in the strain distribution maps indicate tensile strain, while the blue regions indicate compressive strain. The presence of local strain suggests that
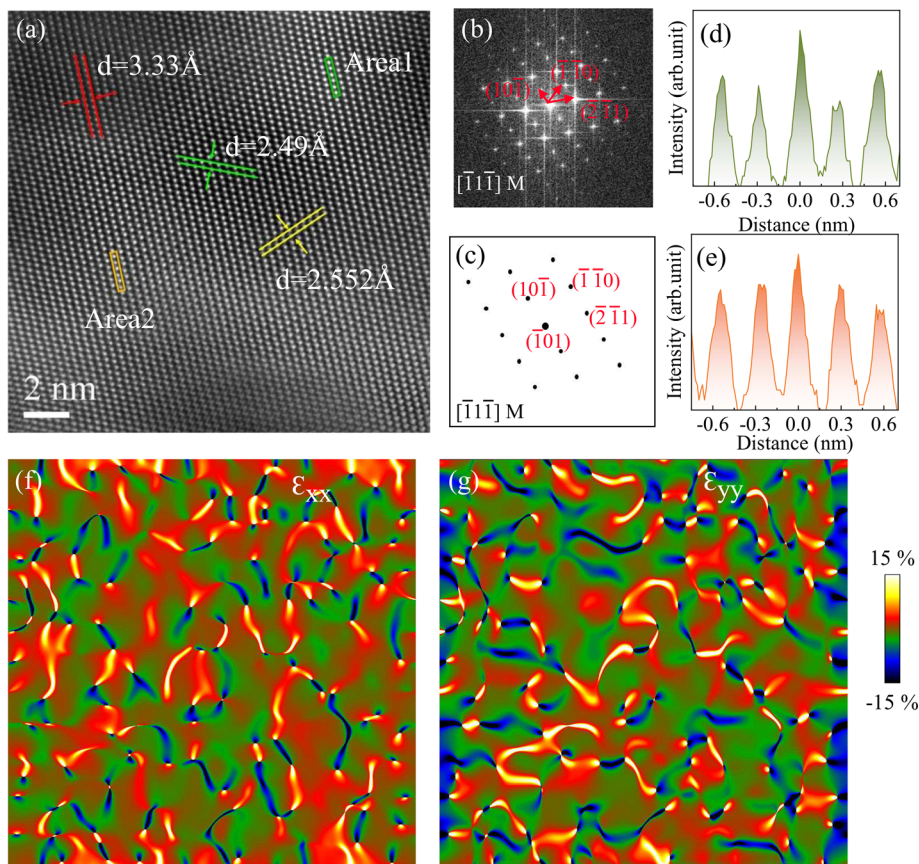
FIG. 2. *In situ* STEM analysis of $Mo_xV_{1-x}O_2$ film (sample S4). (a) High-angle annular dark-field (HAADF) image of the various domains of the $Mo_xV_{1-x}O_2$ film. (b) The FFT image of (a). (c) Simulated diffraction pattern constructed along [–11–1] zone axis, which matches the experimentally obtained FFT image. (d) and (e) The line intensity profiles from area 1 and area 2 in (a). (f) and (g) The corresponding geometric phase analysis (GPA) of (a) in-plane strain (ε_{xx}) and out-of-plane strain (ε_{yy}) map.

the incorporation of Mo atoms leads to lattice distortion and inhomogeneity. These local strains facilitate the transition of VO_2 from the monoclinic to the tetragonal phase, thereby affecting the macroscopic properties.

In Fig. 3, we demonstrate the effect of various Mo doping concentrations on the M1 phase crystal structure and electronic properties of VO_2 by the first-principles calculations. Figures 3(a) and 3(b) are the top and side views of Mo-doped VO_2, respectively. They show the substitution of Mo atoms (purple) for V atoms (green) within the lattice, which results in a stabilized structure. For undoped VO_2 (M1), the electronic structure features a distinct bandgap, exhibiting typical insulating characteristics.[43,44] As shown in Fig. S7, the bandgap arises primarily from the interaction between the V 3d and O 2p orbitals, maintaining VO_2 in an insulating state at room temperature and undergoing an MIT at a specific temperature. Figure 3(c) illustrates the band structures at different Mo doping concentrations. As the doping concentration increases from 3.125% to 12.5%, the energy bands near the Fermi level shift downward (at $E_F = 0$ eV), the bandgap gradually narrows and even disappears, enhancing the metallic properties of VO_2. Particularly at higher doping concentrations (9.375% and 12.5%), the band structure suggests a significant enhancement in the metallic properties of VO_2.

Figure 3(d) further displays the variations in the density of states (DOS) with different Mo doping concentrations. Even at the lowest doping level (3.125%), the bandgap at the Fermi level has vanished,

revealing extended electronic states, which indicates that metallic characteristics have been exhibited at this concentration. With increasing Mo doping, the total density of states at the Fermi level significantly rises, demonstrating stronger metallic traits. The partial density of states from Mo 3d orbitals increases dramatically near the Fermi level, with additional electrons filling the conduction band of VO_2. This results in a dense distribution of electronic states near the Fermi level, which disrupts the stability of the strongly correlated insulating M1 phase and enhances conductivity. Meanwhile, hybridization occurs between the V 3d and O 2p electronic states, reflecting the doping's modulation effect on the overall electronic structure. Therefore, Mo doping significantly alters the electronic structure of VO_2 by providing additional electrons and introducing local lattice distortions, enabling it to exhibit enhanced metallic characteristics at room temperature and thereby suppressing the inherent MIT properties. Moreover, depending on the electronic counting model,[45] the host atoms of ideal $Mo_xV_{1-x}O_2$ are substituted in a Mo electron-rich state, with the Fermi energy level rising into the empty band to metallic (as shown in Fig. S8). The effect remains even at the lowest doping concentration.

In order to deeply investigate Mo-doped VO_2 surface electrical properties at nanoscale, we employed C-AFM to investigate the effect of Mo doping on surface defect states and the behavior of the MIT during heating process. The conductive probe voltage was set to 0.1 V to ensure accuracy and reliability. Figure S9 displays the surface morphology of the $Mo_xV_{1-x}O_2$ film. It can be observed that Mo doping
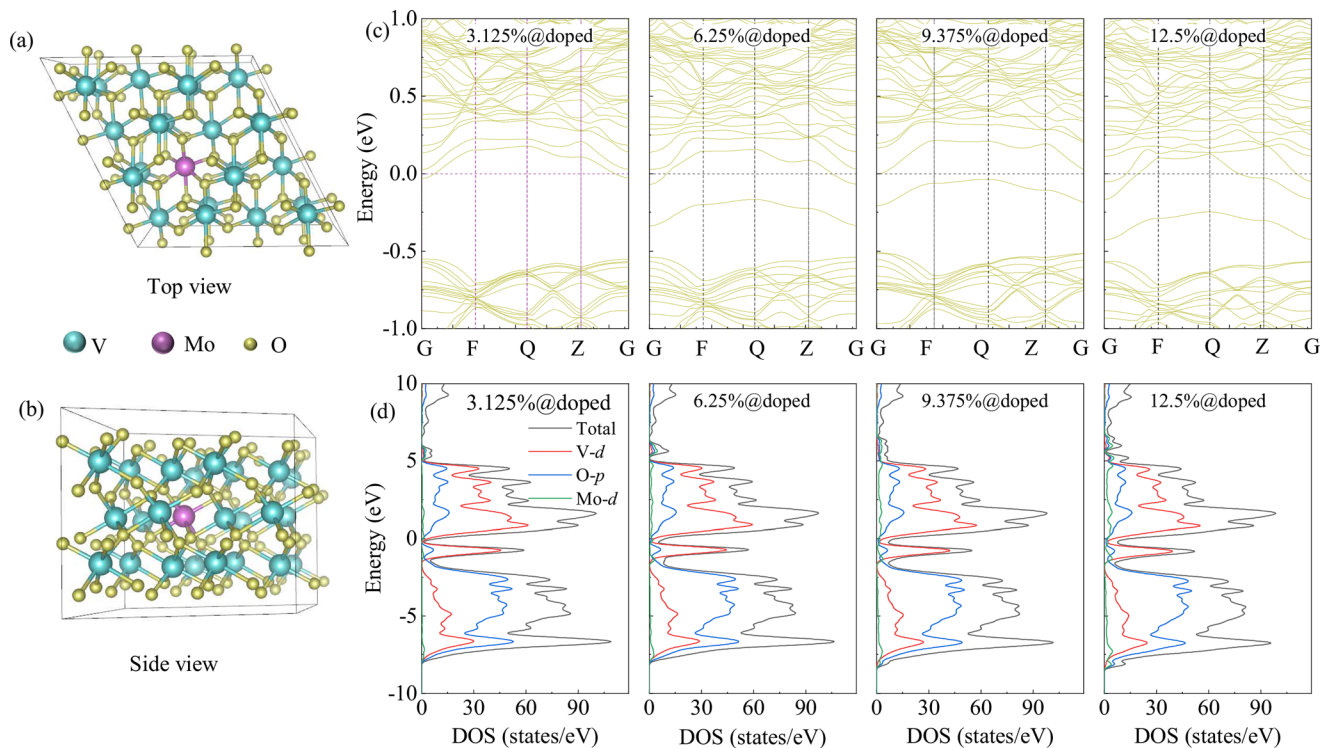
FIG. 3. Band structures and density of states (DOS) of M1 phase Mo-doped VO$_2$. (a) and (b) Schematic diagrams of the crystal structures of the insulator monoclinic structures of Mo$_x$V$_{1-x}$O$_2$. (c) and (d) Band structure and DOS with different Mo doping concentrations at the monoclinic structure, respectively.

increases the size of surface grains, leading to higher surface roughness. The root-mean-square surface roughness was 1.92 nm. Although the Mo doping significantly increases the density of internal defect states, the Mo$_x$V$_{1-x}$O$_2$ films still exhibit an insulating state at room temperature. The randomly distributed high current spots (white bright spots) on the surface of Mo$_x$V$_{1-x}$O$_2$ films can be observed by C-AFM in Fig. 4(a). This phenomenon is attributed to the substantial electron injection into VO$_2$ by Mo^{6+}, which significantly enhances the defect density and disrupts the stability of the M1 phase structure. With the temperature increasing, the thermal motion of free electrons within VO$_2$ intensifies, further increasing the defect density. Correspondingly, as depicted in Figs. 4(a)–4(f), the white bright spots increase in number with rising temperature. The M1 phase structural equilibrium is broken prematurely with the defect density increase, which in turn lowers the T$_{MIT}$. Additionally, the free electrons introduced by Mo^{6+} also play a crucial role in breaking through the strong electron correlation effects. Furthermore, Mo doping weakens the strong correlated electronic effect in VO$_2$, reducing the cooperative effect during the MIT and inhibiting the formation of planar conduction. Compared with undoped VO$_2$ (as shown in Figs. S10 and S11), Mo^{6+} doping introduces free electrons and local defects. These defect regions are more likely to form conductive channels in conductive probe–Mo$_x$V$_{1-x}$O$_2$–Cr electrical circuit, indicating that Mo doping significantly reduces the electron location and suppresses the Mott insulating behavior. This proves that Mo^{6+} can reduce the T$_{MIT}$ of VO$_2$ and make it behave as a LRS on the macroscopic level. However, there are still a few regions where the M1 phase structure has not yet been damaged, remaining in a HRS.

The distribution of the current intensity in Mo$_x$V$_{1-x}$O$_2$ films during the heating process (corresponding to the white dashed line in Fig. 4(a)) is shown in Figs. 4(g)–4(l). It is evident that the defect current produced by Mo doping is relatively small at room temperature. However, as the temperature gradually increases, the number of free electrons generated by oxygen vacancies and Mo^{6+} gradually increases. The thermal field provides substantial energy for free electrons to traverse the internal lattice of VO$_2$, forming the weak conductive channels driven by the nanoscale electric fields. The defect current produced by Mo doping is significantly increased when the temperature reaches 45 °C in Fig. 4(j). This is further evidence that some regions of VO$_2$ have been successfully transformed from M1 phase to R phase under the influence of Mo^{6+}. However, the surface current intensity shows a small decrease when the temperature increases up to 50 °C. This reduction is attributed to the energy from defect states induced by Mo doping being utilized to destabilize the M1 phase structure of VO$_2$, thereby stimulating more regions to transition from the M1 to the R phase. This phenomenon is consistent with the increase in high current areas (white bright spots) observed in Figs. 4(a)–4(f). During the heating process, the resistance significantly reduces as the phase transition occurs from M1 to R phase in Mo$_x$V$_{1-x}$O$_2$ films. Concurrently, the increase in internal defect density facilitates the MIT process, leading to a decrease in the T$_{MIT}$. Despite these changes, C-AFM still reveals the coexistence of metallic and insulating phases at the phase transition temperature. It further demonstrates that the introduction of additional free electrons
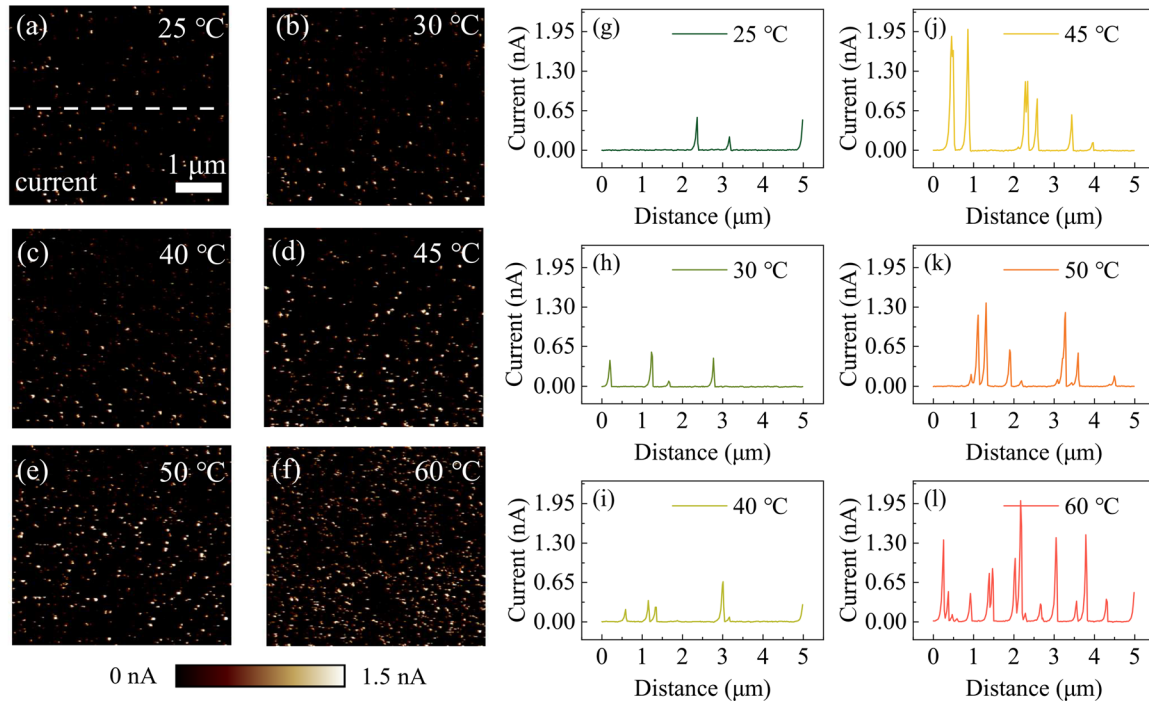
FIG. 4. Variation of the surface electrical properties of $Mo_xV_{1-x}O_2$ films during the heating process, since 25–60 °C. (a)–(f) Plots of surface current intensity at different temperatures. (g)–(l) Plots of current intensity distribution at different temperatures [corresponding to the white dashed line positions in (a)–(f)].

through doping effectively catalyzes the formation of the metallic phase and ensures its predominance.

We used KPFM to study the effects of Mo doping on the surface potential and work function changes of VO_2 during temperature variations. Considering the electrical transport properties in practical scenarios, we tested the $Au–Mo_xV_{1-x}O_2–Au$ region with a channel width of 1.5 μm. Furthermore, we detailed the changes in the VO_2 films before and after Mo doping, with the results displayed in Figs. 5(a) and S12, respectively. Figure 5(b) illustrates the band diagram for $Mo_xV_{1-x}O_2$ contacting Au at room temperature. The presence of Mo^{6+} induces a metal–semiconductor heterojunction between VO_2 and Au, causing significant electron accumulation at the interface. Figures 5(c)–5(h) show the surface potential changes of the $Au–Mo_xV_{1-x}O_2–Au$ areas during the heating. At room temperature, the surface potential difference between $Mo_xV_{1-x}O_2$ and Au is considerably smaller than that of pure VO_2 (as shown in Fig. S13), with a clear potential discontinuity at the interface. With the initial increase in temperature, the decrease in surface potential for $Mo_xV_{1-x}O_2$ in the M1 phase is smaller.

Figure 5(i) shows the distribution of surface potential across the $Au–Mo_xV_{1-x}O_2–Au$ at various temperatures, corresponding to the white dashed line in Fig. 5(c). At room temperature, the potential in the central region of the $Mo_xV_{1-x}O_2$ film remains relatively stable, being primarily affected only at the boundaries. Mo doping increases the electron count on the VO_2 surface, reducing the impact of electron migration from the Au electrodes on the central region and consequently lowering the overall surface potential. This increase in electron density also modifies the work function.

The surface potential of the $Mo_xV_{1-x}O_2$ film (CPD_{VO_2}) and Au (CPD_{Au}) can be defined as[46,47]

$$q \cdot CPD_{VO_2} = W_{tip} - W_{VO_2}, \quad (1)$$

$$q \cdot CPD_{Au} = W_{tip} - W_{Au}, \quad (2)$$

where the W_{tip}, W_{VO_2}, and W_{Au} are the work functions of the conductive probe, the $Mo_xV_{1-x}O_2$ film, and Au, respectively. Moreover, the difference between the W_{VO_2} and W_{Au} can be defined as

$$\Delta W = W_{VO_2} - W_{Au} = q \cdot CPD_{Au} - q \cdot CPD_{VO_2}. \quad (3)$$

Therefore, the ΔW between pure VO_2 film and Au was 71.5 mV (as shown in Fig. S13), which decreased to 21.8 mV after Mo doping at room temperature. Consequently, the work function of $Mo_xV_{1-x}O_2$ is calculated at 5.12 eV, closely approximating that of the R phase of pure VO_2. This indicates that the free electrons introduced by Mo doping significantly alter the electrical properties of the M1 phase VO_2. With increasing temperatures, Mo doping notably reduces the bandgap between the conduction and valence bands, lessening the effect from the temperature on surface potential. When the temperature reaches 45 °C, the coexistence of the M1 and R phases causes a greater reduction in surface potential. At 60 °C, the potential difference between $Mo_xV_{1-x}O_2$ and Au nearly vanishes, with the interface surface potential of $Mo_xV_{1-x}O_2$ even falling below that of Au. This phenomenon is likely due to the transition to a metallic phase and the accumulation of excess electrons introduced by Mo doping at the Au boundary.

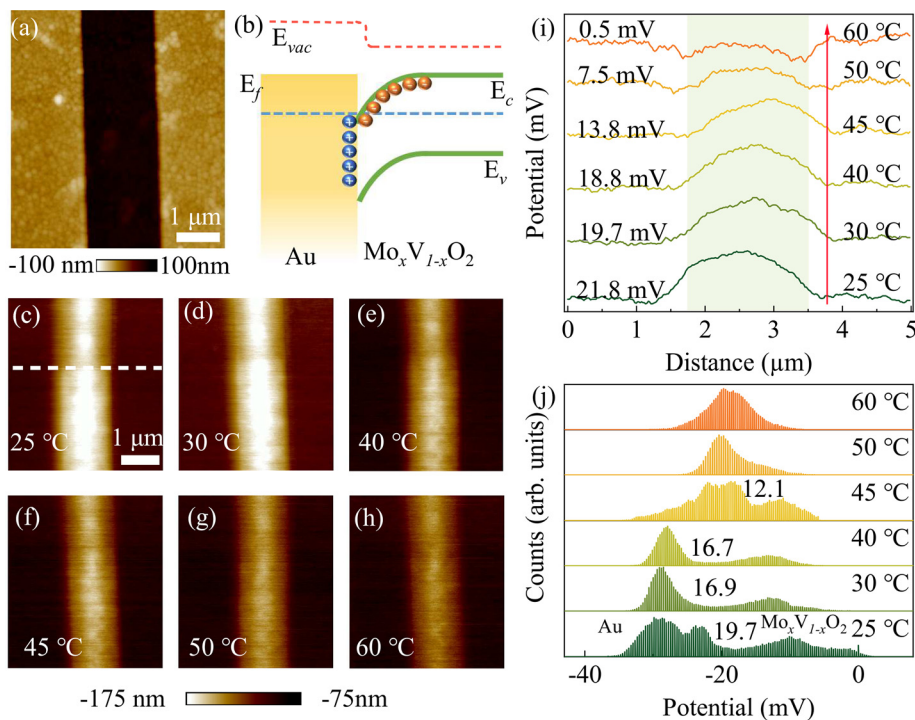Figure 5(j) displays histograms of surface potential for $Au–Mo_xV_{1-x}O_2–Au$ at various temperatures. Compared to undoped VO_2

FIG. 5. Surface potential changes of $Mo_xV_{1-x}O_2$ during the heating process, since 25–60 °C. (a) Surface morphology of the device with a channel width of 1.5 μm. (b) Schematic energy bands of unilateral Au–$Mo_xV_{1-x}O_2$ at room temperature. (c)–(h) Surface potential maps of Au–$Mo_xV_{1-x}O_2$–Au at different temperatures. (i) Au–$Mo_xV_{1-x}O_2$–Au surface potential distribution curve during the heating process [corresponding to the position of the white dashed line in (c)]. (j) Histogram of surface potentials.

(as shown in Fig. S14), the potential peak of $Mo_xV_{1-x}O_2$ becomes more pronounced and gradually approaches the potential peak of the Au electrode as the temperature increases. At 45 °C, the Au potential peak splits. This split is due to a localized transition from an insulating to a metallic phase in $Mo_xV_{1-x}O_2$, causing both phases to coexist. The peak to the right of the Au peak still represents the insulating phase. This histogram of the potential distribution also explains the enhancement of the surface current measured at 45 °C in the C-AFM test. As the temperature continues to rise, the potential of $Mo_xV_{1-x}O_2$ approaches that of Au closely, leading to the merging of the peaks. This makes it difficult to distinguish the separation between the peaks.

Mo-doped VO_2 thin films exhibit significant potential for applications in selectors and volatile memory due to their high temperature sensitivity, lower T_{MIT}, and broader hysteresis loops. In practical applications, the durability, selectivity, stability, and reliability are the most important performance indicators of the selectors. Therefore, to further demonstrate the superior performance of Mo-doped VO_2 thin films in selectors, we designed a simple and operable switching device in Fig. 6(a). This device utilizes Cr/Au as the top electrode with a channel width of 1.5 μm. A detailed optical image of a single device is presented in Fig. 6(b), where the thicknesses of the Cr/Au electrodes and the $Mo_xV_{1-x}O_2$ layer are measured at 110 and 90 nm, respectively. We conducted over 1000 consecutive I–V cycles on this device (−3 V to 3 V) at various temperatures, and the results are summarized in Fig. 6(c). The device exhibits symmetric I–V characteristics and significant nonlinear switching behavior, activating threshold switch characteristics without the need for an initial voltage. This phenomenon depends on the MIT characteristics. Upon reaching the threshold voltage, the material quickly switches from the HRS to the LRS and optimizes the formation of conductive channels by appropriate Mo

doping. It is noticed that the device switches to the LRS with a threshold voltage (V_{th}) of about 2.25 V at 25 °C in Fig. 6(f), while the current significantly drops at a holding voltage (V_{hold}) of about 1.25 V during the reverse scan, marking the transition back to the HRS.

Figure 6(d) displays the cumulative plots of the threshold and hold voltage over 1000 repetitive cycles at room temperature, including V_{th-pos}, V_{th-neg}, $V_{hold-pos}$, and $V_{hold-neg}$. These results demonstrate the device's stability across 1000 cycles, confirming its robust endurance under repeated cycling conditions. Through statistical analysis, we calculated the coefficient of variation (C_v), defined as the ratio of the standard deviation (σ) to the mean value (μ), $C_v = (\sigma/\mu) \times 100\%$ (as shown in Fig. S15). The results show C_v values of 2.85%, 1.40%, 0.89%, and 0.81% for V_{th-pos}, V_{th-neg}, $V_{hold-pos}$, and $V_{hold-neg}$, respectively, indicating excellent cycle-to-cycle (C2C) consistency and high stability.[17] These low C_v values underscore the reliability, and the high uniformity of the devices can be attributed to the high crystallinity of $Mo_xV_{1-x}O_2$, as well as the maintenance of ideal dimensions and thickness in the planar device structure. The crosstalk between adjacent unselected cells poses a direct threat to data integrity and operational accuracy in selectors arrays, limiting the increase in storage capacity per unit area and impeding the execution of complex logic operations and the maintenance of network stability. Figure 6(e) demonstrates the 1000 cycles resistance values of the selectors with a reading voltage (V_{read}) of 1.4 V and a half-read voltage ($V_{read/2}$) of 0.7 V in LRS and HRS, respectively. It can be seen that the difference in resistance between the HRS and LRS of the selectors remains significant at room temperature, indicating good switching characteristics of the device with no significant performance degradation. Additionally, the selectivity is $>10^2$ at room temperature. This pronounced threshold switching characteristic can be attributed to Joule heating-induced MIT
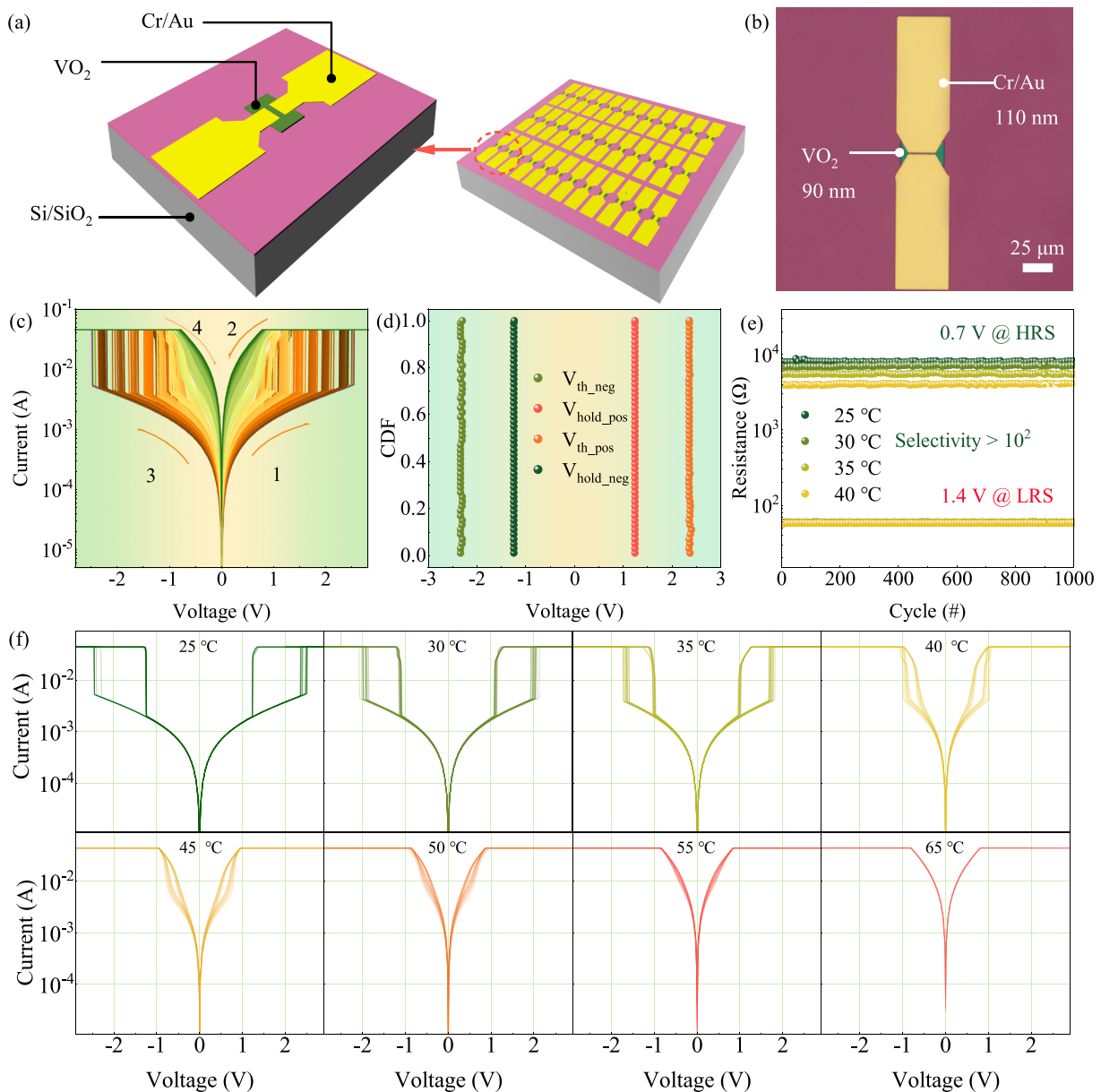
FIG. 6. Characteristics of $Mo_xV_{1-x}O_2$ selectors. (a) Schematic diagram of the device, which is a planar structure. (b) Optical image of the signal device. (c) Overall I–V characteristics of $Mo_xV_{1-x}O_2$ selectors over than 1000 cycles at different temperature, since 25–100 °C. (d) Cumulative plots of negative threshold (V_{th-neg}), positive threshold (V_{th-pos}), negative holding threshold ($V_{hold-neg}$), and positive holding threshold ($V_{hold-pos}$) at room temperature. (e) Cycling characteristics of $Mo_xV_{1-x}O_2$ selectors in high-resistance state (HRS) and low-resistance state (LRS) at different temperatures. (f) Cycling I–V characteristics at different temperatures.

between the electrodes. Furthermore, as the temperature increases, the selectivity of the device gradually decreases, primarily due to an increase in current in the HRS. The rise in temperature reduces the thermal energy required for the phase transition, leading to a decrease in the phase transition barrier, threshold window, and V_{th} (as shown in Fig. S16). When the temperature exceeds the phase transition temperature, the device fully enters the metallic state, and the current no longer changes in the LRS, thus losing its threshold characteristics.

IV. CONCLUSION AND OUTLOOK

In summary, we successfully demonstrated the impact of Mo doping on the lattice structure and electrical properties of VO_2. The atomic-resolution study of Mo-doped VO_2 thin films reveals that the Mo dopant does not disrupt the VO_2 crystal structure but introduces local strain within the monoclinic (−101) lattice plane. This local lattice distortion accelerates the phase transition from the monoclinic to the tetragonal phase. Furthermore, we employed C-AFM and KPFM

to precisely characterize these changes at the nanoscale, revealing the direct effects of Mo doping on the electronic structure and phase transition behavior of VO_2 films. The results indicate that the introduction of a significant number of electrons by Mo^{6+} substantially disrupts the stability of the M1 phase of VO_2, effectively suppressing the strong electron correlation effects described by the Mott model.

Additionally, we identified a specific concentration with a lower phase transition temperature ($T_h = 55.8\,°C$) and a broader hysteresis window ($\Delta T = 13.6\,°C$) to explore its potential applications in selectors and other volatile memory devices. The optimized Mo-doped VO_2 films exhibited excellent threshold and memristive properties at room temperature, capable of rapidly switching from the HRS to the LRS at V_{th} of 2.37 V. This stable switching performance, along with high selectivity ($>10^2$), significantly enhances its potential for practical applications. After more than 1000 cycles, the material demonstrated outstanding durability and reliability, providing strong evidence for its use in future high-performance electronic devices.

SUPPLEMENTARY MATERIAL

See the supplementary material for more fundamental characterizations of $Mo_xV_{1-x}O_2$ films, (log(R))/dT curves of all $Mo_xV_{1-x}O_2$ films, DOS and band structure of undoped VO_2, Fermi energy level of different Mo atom count, AFM morphology of the typical $Mo_xV_{1-x}O_2$ film, discussion of C-AFM and KPFM measurements of pure VO_2 film, and additional electrical measurements.

ACKNOWLEDGMENTS

AUTHOR DECLARATIONS
Conflict of Interest

The authors have no conflicts to disclose.

Author Contributions

Lin Wang: Conceptualization (lead); Data curation (lead); Formal analysis (lead); Writing – original draft (lead). **Li Chen:** Formal analysis (equal); Investigation (equal). **Xionghu Xu:** Formal analysis (supporting). **Zhangchen Hou:** Formal analysis (supporting). **Yafang Li:** Formal analysis (supporting). **Liyan Shang:** Formal analysis (supporting). **Jinzhong Zhang:** Formal analysis (supporting). **Liangqing Zhu:** Formal analysis (supporting). **Yawei Li:** Formal analysis (supporting). **Fei Cao:** Validation (equal). **Genshui Wang:** Formal analysis (equal). **Junhao Chu:** Supervision (equal). **Zhigao Hu:** Conceptualization (equal); Funding acquisition (lead); Project administration (lead); Supervision (equal); Writing – review & editing (lead).

DATA AVAILABILITY

The data that support the findings of this study are available from the corresponding author upon reasonable request.

REFERENCES

[1]N. Shen, S. Chen, W. Wang, R. Shi, P. Chen, D. Kong, Y. Liang, A. Amini, J. Wang, and C. Cheng, J. Mater. Chem. A **7**(9), 4516–4524 (2019).

[2]S. H. Bae, S. Lee, H. Koo, L. Lin, B. H. Jo, C. Park, and Z. L. Wang, Adv. Mater. **25**(36), 5098 (2013).

[3]Y. J. Lee, Y. Kim, H. Gim, K. Hong, and H. W. Jang, Adv. Mater. **36**(5), 2305353 (2023).

[4]N. Manca, T. Kanki, F. Endo, E. Ragucci, L. Pellegrino, and D. Marré, ACS Appl. Electron. Mater. **3**(1), 211–218 (2021).

[5]C.-Y. Lin, P.-H. Chen, T.-C. Chang, K.-C. Chang, S.-D. Zhang, T.-M. Tsai, C.-H. Pan, M.-C. Chen, Y.-T. Su, Y.-T. Tseng, Y.-F. Chang, Y.-C. Chen, H.-C. Huang, and S. M. Sze, Nanoscale **9**(25), 8586–8590 (2017).

[6]N. B. Aetukuri, A. X. Gray, M. Drouard, M. Cossale, L. Gao, A. H. Reid, R. Kukreja, H. Ohldag, C. A. Jenkins, E. Arenholz, K. P. Roche, H. A. Dürr, M. G. Samant, and S. S. P. Parkin, Nat. Phys. **9**(10), 661–666 (2013).

[7]U. Dilna and S. N. Prasad, Mater. Sci. Semicond. Process. **171**, 108008 (2024).

[8]G. R. Khan, K. Asokan, and B. Ahmad, Thin Solid Films **625**, 155–162 (2017).

[9]H. Yu, A. N. M. N. Islam, S. Mondal, A. Sengupta, and S. Ramanathan, IEEE Trans. Electron Devices **69**(6), 3135–3141 (2022).

[10]J. Lappalainen, J. Mizsei, and M. Huotari, J. Appl. Phys. **125**(4), 044501 (2019).

[11]J. Y. Son and Y. H. Shin, Appl. Phys. Lett. **92**(22), 222106 (2008).

[12]Y. Chen, Y. Zhang, Z. Wang, T. Zhan, Y. C. Wang, H. Zou, H. Ren, G. Zhang, C. Zou, and Z. L. Wang, Adv. Mater. **30**(45), 45 (2018).

[13]L. Pellegrino, N. Manca, T. Kanki, H. Tanaka, M. Biasotti, E. Bellingeri, A. S. Siri, and D. Marré, Adv. Mater. **24**(21), 2929–2934 (2012).

[14]Y. Wang, L. Seewald, Y. Y. Sun, P. Keblinski, X. Sun, S. Zhang, T. M. Lu, J. M. Johnson, J. Hwang, and J. Shi, Adv. Mater. **28**(40), 8975–8982 (2016).

[15]M. K. Dietrich, F. Kuhl, A. Polity, and P. J. Klar, Appl. Phys. Lett. **110**(14), 141907 (2017).

[16]H. Ma, J. Hou, X. Wang, J. Zhang, Z. Yuan, L. Xiao, Y. Wei, S. Fan, K. Jiang, and K. Liu, "Flexible," Nano Lett. **17**(1), 421–428 (2017).

[17]R. Yuan, P. J. Tiw, L. Cai, Z. Yang, C. Liu, T. Zhang, C. Ge, R. Huang, and Y. Yang, Nat. Commun. **14**(1), 3695 (2023).

[18]K. Yang, Y. Wang, P. J. Tiw, C. Wang, X. Zou, R. Yuan, C. Liu, G. Li, C. Ge, S. Wu, T. Zhang, R. Huang, and Y. Yang, Nat. Commun. **15**(1), 1693 (2024).

[19]Y. Zhao, J. Hao, C. Chen, and Z. Fan, J. Phys. Condens. Matter **24**(3), 035601 (2012).

[20]J. Zhang, Z. Zhao, J. Li, H. Jin, F. Rehman, P. Chen, Y. Jiang, C. Chen, M. Cao, and Y. Zhao, ACS Appl. Mater. Interfaces **9**(32), 27135–27141 (2017).

[21]P. Schofield, A. Bradicich, R. M. Gurrola, Y. Zhang, T. D. Brown, M. Pharr, P. J. Shamberger, and S. Banerjee, Adv. Mater. **35**(37), 2205294 (2022).

[22]S. M. Bohaichuk, M. Muñoz Rojo, G. Pitner, C. J. McClellan, F. Lian, J. Li, J. Jeong, M. G. Samant, S. S. P. Parkin, H. S. P. Wong, and E. Pop, ACS Nano **13**(10), 11070–11077 (2019).

[23]H. Asayesh-Ardakani, A. Nie, P. M. Marley, Y. Zhu, P. J. Phillips, S. Singh, F. Mashayek, G. Sambandamurthy, K.-B. Low, R. F. Klie, S. Banerjee, G. M. Odegard, and R. Shahbazian-Yassar, Nano Lett. **15**(11), 7179–7188 (2015).

[24]M. Pattanayak, M. N. F. Hoque, Y.-C. Ho, W. Li, Z. Fan, and A. A. Bernussi, Appl. Mater. Today **30**, 101642 (2023).

[25]C. Ling, Z. Zhao, X. Hu, J. Li, X. Zhao, Z. Wang, Y. Zhao, and H. Jin, ACS Appl. Nano Mater. **2**(10), 6738–6746 (2019).

[26]J. A. J. Rupp, R. Waser, and D. J. Wouters, in *IEEE 8th International Memory Workshop (IMW)* (IEEE, 2016).

[27]N. Émond, A. Ibrahim, B. Torriss, A. Hendaoui, I. Al-Naib, T. Ozaki, and M. Chaker, Appl. Phys. Lett. **111**(9), 092105 (2017).

[28]Z. Yang, C. Ko, V. Balakrishnan, G. Gopalakrishnan, and S. Ramanathan, Phys. Rev. B **82**(20), 205101 (2010).

[29]F. Chen, L. Yuan, X. Wu, Y. Huang, Y. Wang, and X. Weng, Ceram. Int. **49**(15), 25585–25593 (2023).

[30]Y. Li, J. Chen, L. Su, X. Zhang, Q. Zheng, Y. Huo, and D. Lin, J. Colloid Interface Sci. **652**, 440–448 (2023).

[31]G. Kresse and J. Hafner, Phys. Rev. B **47**(1), 558–561 (1993).

[32]B. Liu, K. Tang, K. Song, P. A. van Aken, Y. Yu, J. Maier, M. K. Song, and P. van Aken, Phys. Rev. B **49**, 16223–16233 (1994).

[33]P. E. Blöchl, Phys. Rev. B **50**(24), 17953–17979 (1994).

[34]J. P. Perdew, K. Burke, and M. Ernzerhof, Phys. Rev. Lett. **77**, 3865 (1996).

[35]S. L. Dudarev, G. A. Botton, S. Y. Savrasov, C. J. Humphreys, and A. P. Sutton, Phys. Rev. B **57**(9), 1505 (1998).

[36]S. Biermann, A. Poteryaev, A. I. Lichtenstein, and A. Georges, Phys. Rev. Lett. **94**(2), 026404 (2005).

[37]J. Wei, H. Ji, W. Guo, A. H. Nevidomskyy, and D. Natelson, Nat. Nanotechnol. **7**(6), 357–362 (2012).

[38]H. J. Monkhorst and J. D. Pack, Phys. Rev. B **13**(12), 5188–5192 (1976).

[39]S. Amador-Alvarado, J. M. Flores-Camacho, A. Solis-Zamudio, R. Castro-García, J. S. Përez-Huerta, E. Antúnez-Cerõn, J. Ortega-Gallegos, J. Madrigal-Melchor, V. Agarwal, and D. Ariza-Flores, Sci. Rep. **10**(1), 2045 (2020).

[40]L. Wang, M. H. Deng, X. H. Xu, Z. C. Hou, M. Li, L. Chen, A. Y. Cui, K. Jiang, L. Y. Shang, J. H. Chu, and Z. G. Hu, Adv. Opt. Mater. **11**(22), 2300854 (2023).

[41]Z. Zhang, F. Zuo, C. Wan, A. Dutta, J. Kim, J. Rensberg, R. Nawrodt, H. H. Park, T. J. Larrabee, X. Guan, Y. Zhou, S. M. Prokes, C. Ronning, V. M. Shalaev, A. Boltasseva, M. A. Kats, and S. Ramanathan, Phys. Rev. Appl. **7**, 2331–7019 (2017).

[42]V. Grillo and F. Rossi, Ultramicroscopy **125**, 112–129 (2013).

[43]L. Wang, Y.-Q. Hao, W. Ma, and S. Liang, Rare Met. **40**(5), 1337–1346 (2021).

[44]D. Lee, T. Min, G. Lee, J. Kim, S. Song, J. Lee, J. S. Bae, H. Kang, J. Lee, and S. Park, J. Phys. Chem. Lett. **11**(22), 9680–9688 (2020).

[45]L. Chen, L. Wang, K. Jiang, J. Z. Zhang, Y. W. Li, L. Y. Shang, L. Q. Zhu, S. J. Gong, and Z. G. Hu, J. Phys. Chem. Lett. **14**(25), 5760–5767 (2023).

[46]A. Sohn, H. Kim, D.-W. Kim, C. Ko, S. Ramanathan, J. Park, G. Seo, B.-J. Kim, J.-H. Shin, and H.-T. Kim, Appl. Phys. Lett. **101**(19), 191605 (2012).

[47]A. Sohn, H. Kim, D.-W. Kim, C. Ko, S. Ramanathan, J. Park, G. Seo, B.-J. Kim, J.-H. Shin, and H.-T. Kim, Appl. Phys. Lett. **107**(10), 171603 (2015).

01 February 2025 03:49:23